Insight into the Mechanisms of High Activity and Stability of Iridium Supported on Antimony-Doped Tin Oxide Aerogel for Anodes of Proton Exchange Membrane Water Electrolyzers

Viktoriia Saveleva, Li Wang, Olga Kasian, Maria Batuk, Joke Hadermann, Jean-Jacques Gallet, Fabrice Bournel, Nicolas Alonso-Vante, Guillaume Ozouf, Christian Beauger, et al.

To cite this version:

Viktoriia Saveleva, Li Wang, Olga Kasian, Maria Batuk, Joke Hadermann, et al.. Insight into the Mechanisms of High Activity and Stability of Iridium Supported on Antimony-Doped Tin Oxide Aerogel for Anodes of Proton Exchange Membrane Water Electrolyzers. ACS Catalysis, 2020, 10 (4), pp.2508-2516. 10.1021/acscatal.9b04449 . hal-03884348

HAL Id: hal-03884348
https://hal.science/hal-03884348

Submitted on 3 May 2024

Insight into the mechanisms of high activity and stability of iridium supported on antimony-doped tin oxide aerogel for anodes of proton exchange membrane ater electrolyzers

Reference:

Saveleva V.A., Wang L., Kasian O., Batuk Maria, Hadermann Joke, Gallet J.-J., Bournel F., Alonso-Vante N., Ozouf G., Beauger C., ...- Insight into the mechanisms of high activity and stability of iridium supported on antimony-doped tin oxide aerogel for anodes of proton exchange membrane ater electrolyzers
ACS catalysis - ISSN 2155-5435 - 10:4(2020), p. 2508-2516
Full text (Publisher's DOI): https://doi.org/10.1021/ACSCATAL.9B04449
To cite this reference: https://hdl.handle.net/10067/1671470151162165141

Insight into the Mechanisms of High Activity and Stability of Iridium Supported on Antimony-Doped Tin Oxide Aerogel for Anodes of Proton Exchange Membrane Water Electrolysers

V. A. Saveleva[a†]*, L. Wang[b], O. Kasian[c,d], M. Batuk[e], J. Hadermann[e], J.-J. Gallet[f,g], F. Bournel[f,g], N. Alonso-Vante[h], G. Ozouf[i], C. Beauger[i], K. J.J. Mayrhofer[c,j], S. Cherevko[c,j], A. S. Gago[b]*, K. A. Friedrich[b,k], S. Zafeiratos[a] and E. R. Savinova[a]

---

[a] *Institut de Chimie et Procédés pour l'Energie, l'Environnement et la Santé, UMR 7515 du CNRS-Université de Strasbourg, 25 Rue Becquerel, 67087 Strasbourg, France*

[b] *Institute of Engineering Thermodynamics, German Aerospace Center (DLR), Pfaffenwaldring 38-40, Stuttgart, 70569, Germany.*

[c] *Helmholtz-Zentrum Berlin GmbH, Helmholtz-Institute Erlangen-Nürnberg, 14109 Berlin, Germany*

[d] *Max-Planck-Institut für Eisenforschung GmbH, Max-Planck-Straße 1, 40237 Düsseldorf, Germany*

[e] *EMAT, University of Antwerp, Department of Physics, Groenenborgerlaan 171, 2020 Antwerp, Belgium.*

[f] *Laboratoire de Chimie Physique-Matière et Rayonnement, Sorbonne Universités – UPMC Univ Paris 06 – CNRS, 4 place Jussieu, 75005 Paris, France.*

[g] *Synchrotron-Soleil, L'orme des Merisiers, Saint Aubin – BP48 91192 Gif-sur-Yvette Cedex, France.*

[h] *IC2MP - UMR-CNRS 7285, Université de Poitiers, 4, rue Michel Brunet - B27 BP 633 - TSA 51106, F-86022 Poitiers Cedex, France*

[i] *MINES ParisTech, PSL University, Centre for processes Renewable Energy and Energy Systems (PERSEE),), CS 10207, Rue Claude Daunesse, F-06904, Sophia-Antipolis Cedex, France*

[j] *Helmholtz-Institute Erlangen-Nürnberg for Renewable Energy (IEK-11), Forschungszentrum Jülich GmbH, Egerlandstr. 3, 91058, Erlangen, Germany*

[k] *Institute of Building Energetics, Thermal Engineering and Energy Storage (IGTE), University of Stuttgart, Pfaffenwaldring 31, 70569 Stuttgart 70569, Germany.*

[†]*current address: Electrochemistry Laboratory, Paul Scherrer Institut, 5232 Villigen, Switzerland*

*E-mail: aldo.gago@dlr.de; viktoriia.saveleva@psi.ch

Abstract

The use of high amounts of iridium in industrial proton exchange membrane water electrolysers (PEMWE) could hinder their widespread use for the decarbonisation of society with hydrogen. Non-thermally oxidised Ir nanoparticles supported on antimony-doped tin oxide (SnO_2:Sb, ATO) aerogel allow decreasing the use of the precious metal by more than 70 %, while enhancing the electro-catalytic activity and stability. To date the origin of these benefits remains unknown. Here we present clear evidence on the mechanisms that lead to the enhancement of the electrochemical properties of the catalyst. *Operando* near ambient pressure X-ray photoelectron spectroscopy on membrane electrode assemblies reveals a low degree of Ir oxidation, attributed to the oxygen spill-over from Ir to SnO_2:Sb. Furthermore, the formation of highly unstable Ir(III) species is mitigated, while the decrease of Ir dissolution in Ir/SnO_2:Sb is confirmed by inductively coupled plasma mass spectrometry (ICP-MS). The mechanisms that lead to the high activity and stability of Ir catalyst supported on SnO_2:Sb aerogel for PEMWE are thus unveiled.

Keywords: iridium, oxygen evolution reaction, operando photoelectron spectroscopy, antimony-doped tin oxide, reaction mechanism

Green hydrogen is one of the most promising solutions for the decarbonisation of society. It can be produced by water electrolysis using renewable electricity. Currently, two technologies, i.e. alkaline and proton exchange membrane water electrolysis (PEMWE) are equally considered. Alkaline water electrolysis is already a mature technology, but its successful integration with intermittent renewables is still to be proven. Challenges to be overcome are related to safe and reliable operation at highly dynamic loads. On the other hand, operation of PEMWE together with renewables has been numerously demonstrated, including industrial applications, but its dependence on iridium poses a serious threat for up-scaling.

In recent years, the deployment of PEMWE for hydrogen production in large industrial applications has been rapidly increasing. In 2012, Hydrogenics announced the construction of the first 1 MW PEMWE for Power-to-Gas and started operation in 2014[1]. A year earlier Siemens commissioned a 6 MW PEMWE in Mainz Energy Park, Germany. In 2018, Shell announced the installation of a 10 MW PEMWE in a refinery[2] and in 2019 Air Liquide acquired a 20 MW PEMWE for supplying hydrogen in one of their chemical plants. Air Liquide, which is one of the largest hydrogen companies, has made a commitment to produce at least 50% of their hydrogen through carbon-free processes such as electrolysis by 2020[3]. Other large hydrogen industries such as Shell, Repsol and Thyssenkrupp have announced similar targets for reducing their CO_2 emissions. Recently, Amprion and Open Grid Europe announced the first 100 MW electrolyser for power-to-gas[4]. Based on these trends, it is very likely that in the next 5 years the 100 MW scale PEMWE will be the base system for supplying green hydrogen to the oil, chemical and steel industry.

However, the use of Ir at the anode of PEMWE where a kinetically sluggish oxygen evolution reaction, OER, occurs, may slow down dramatically the rapid growth of this technology. Indeed, a 100 MW PEMWE requires about 50 kg of Ir, assuming the current loadings of 2 mg cm^{-2} and a current density of 2 A cm^{-2}. For most PEMWE companies, the Ir and Pt catalysts comprised about 5-10% of the stack cost[5,6].

However, the price of Ir has reached historical levels being 40,000 Euro/kg, doubling the 2014 price[7] when the first MW-size PEMWE were constructed. Recently, it has been reported a significant cost reduction of 55% in the stack cost, which was mainly due to the bipolar plates[8]. After this reduction, the MEA (membrane and precious metal catalysts) appeared as the most expensive stack component. If the price of the precious metal continues increasing at the rate observed in the last five years[9], it could hinder the widespread of the PEMWE technology at large scale in the near future. Therefore, there is an urgent need for reducing the amount of Ir in the anodes of large scale PEMWE stacks, without compromising their efficiency and durability.

In order to improve the mass-weighted activity of iridium, several strategies are currently pursued, such as decreasing the particle size[10], developing core-shell structures,[11,12] replacing less active crystalline by more active amorphous Ir oxide,[13,14] selective leaching of a less stable component to produce highly active nanoporous materials,[11,12], or supporting Ir nanoparticles on conductive supports[11,15–17]. Electrochemically oxidized Ir exhibits more than a hundred times higher OER activity compared to thermally oxidized crystalline rutile-type structured IrO_2[18], but is much less stable[19,20]. In addition, the highly active amorphous phase slowly recrystallizes into its less active crystalline counterpart.[21] It is thus a challenge to stabilize highly active and finely dispersed electrochemically oxidized Ir nanoparticles in order to increase the lifetime of PEMWE anodes.

While carbon-supported materials are routinely used in fuel cell technology, their use is not possible at the anodes of PEMWE due to carbon corrosion. Considering this, oxide-based supports such as TiO_2,[22,23] Magnéli phases Ti_4O_7[17,24], WO_3[25] or Sb-doped SnO_2 (SnO_2:Sb) [15,26–31,] have been proposed. Among these, SnO_2:Sb is considered as one of the most promising support materials for OER catalysts. The use of SnO_2:Sb -supported Ir allows reducing the precious metal by more than 70% while keeping the same OER current per unit geometric surface area[30]. While an increase of the mass-specific activity and stability of SnO_2:Sb -supported Ir catalysts has been documented by several groups[30,32], its origin is barely understood.

Oh et al.[15] applied a combination of spectroscopic techniques, including X-ray absorption spectroscopy and XPS (X-ray photoelectron spectroscopy) to compare IrO_x/C and IrO_x/SnO_2:Sb catalysts subjected to electrochemical oxidation. The authors observed that the apparent oxidation state of iridium is lower in IrO_x/SnO_2:Sb than in IrO_x/C, resp. +3.2 versus +4, and that in Ir/SnO_2:Sb the effective IrO_x layer thickness is smaller. They attributed these differences to a charge transfer from SnO_2:Sb to the IrO_x nanoparticles and proposed that corrosion stability of the latter significantly benefits from a strong integration with the SnO_2:Sb support. *Lluis et al.*[32] recently compared the OER activity and stability of unsupported and doped-SnO_2 aerogels supported Ir nanoparticles. The latter revealed to be both more active and stable. However, no clear explanation was given regarding the stabilisation mechanism. Moreover, the study was carried out *ex situ*, on model electrodes with a liquid electrolyte which might not be representative of the real environment of a PEMWE.

Here we present an *operando* study of a PEMWE having a membrane electrode assembly with Ir/SnO_2:Sb anode by means of near-ambient pressure XPS (NAP-XPS). The analysis of photoemission spectra recorded under polarisation in water vapor ambient allows us to follow the evolution of the iridium oxidation state. NAP-XPS data on Ir/SnO_2:Sb are compared with the recently published data obtained from similar experiments for unsupported Ir.[20,33]

Furthermore, the results evidence a diminution of the Ir(III) fraction, the latter being considered an intermediate in the Ir dissolution process. Inductively coupled plasma mass spectrometry (ICP-MS) confirms the decrease in the dissolution rate of Ir in Ir/SnO_2:Sb electrodes.

Data interpretation is complemented by high resolution transmission electron microscopy (HR TEM), high-angle annular dark-field scanning transmission electron microscopy (HAADF-STEM) and STEM coupled with the energy-dispersive X-ray spectroscopy (STEM-EDX) analysis of pristine and post-mortem catalyst samples.

Surface state of Ir: insights from *operando* NAP-XPS. The SnO_2:Sb-supported Ir catalyst integrated in a membrane electrode assembly (MEA) was studied with NAP-XPS at room temperature (RT) and 3 mbar H_2O vapour pressure in the potential interval (here and in what follows the electrode potential is Ohmic drop corrected) from 0.2 till 1.7 V vs. dynamic hydrogen electrode (DHE). Cyclic voltammogram (Figure 1A) and current transients (Figure 1B) show OER currents above ca. 1.4 V (similar to what has been observed in a liquid electrolyte[30]) confirming that the experimental conditions are compatible with those applied during water electrolysis. The Ir4f core level spectrum (Figure 1C) acquired at 0.2 V is dominated by the doublet of metallic Ir (binding energy of $Ir4f_{7/2}$ = 60.7 eV), despite the fact that the Ir/SnO_2:Sb electrode was subjected to potential cycling in the interval from 0.2 to 1.0 V before NAP-XPS measurements. As the anodic polarisation is increased, Ir4f spectra gradually change (see Ir4f spectrum at 1.7 V in Figure 1D), demonstrating an increase of the photoemission peak intensity at 62.0 and 65.0 eV, corresponding to the Ir(IV) doublet. While the binding energy of the Ir doublets is potential-independent, the Sn3d peaks shift slightly to lower binding energy values (Figure 1E). The origin of this binding energy shift will be discussed in more detail in the next section.

To unveil the influence of the SnO_2:Sb support on the oxidation state of iridium, we compare Ir4f XP spectra for Ir/SnO_2:Sb (Figure 2A, D) with those of an unsupported iridium catalyst (Figure 2B, E) acquired in 3 mbar H_2O ambient in the same experimental set-up[33] at SOLEIL synchrotron and at the potential close to the open-circuit at different kinetic energies, representing different analytical depth (see Table S4). In order to exclude the strong reduction of the metal oxides under the incident beam several measures have been taken such as closed beam shutter as well as the temporal evolution of the spectra was constantly followed. The spectra for the SnO_2:Sb -supported differ considerably from those for the unsupported Ir. While for the unsupported catalyst the Ir4f XP spectra at low potentials clearly show contributions from three oxidation states, i.e. metallic Ir, Ir(III) and Ir(IV), for Ir/SnO_2:Sb the spectra are dominated by the doublet of metallic Ir, and demonstrate a small contribution of Ir(IV), and a negligible amount of Ir(III) (see Panel C of Figure

1). Due to the act, that both supported and unsupported iridium catalysts have been analyzed using the same measurement protocols including the conditioning of the catalyst and the same photon energies, in the case of strong radiation damage, both unsupported Ir and Ir/ATO catalysts should be reduced what is not the case. Based on this, we attribute the differences in Ir oxidation observed during our measurements at SOLEIL mostly to the presence of support.

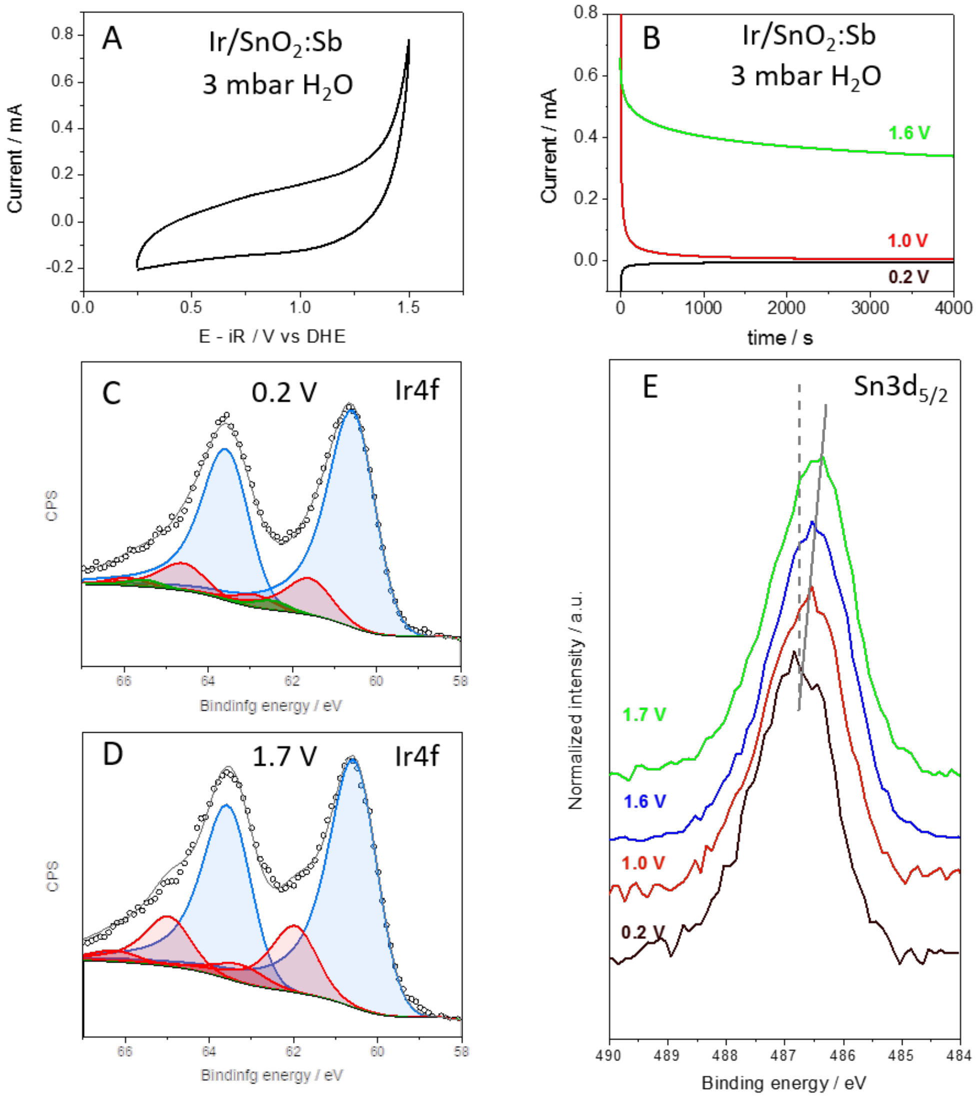

Figure 1. *CV (A) and chronoamperograms (B) of Ir/SnO_2:Sb in NAP-XPS chamber. Ir4f (C, D) and Sn3d$_{5/2}$ (E) XP spectra recorded on Ir/SnO_2:Sb -based anode. Colour codes: metallic Ir –blue, Ir(IV) and its satellite – red, Ir (III) - green. Experimental results are shown as circles, fitting as a grey line. The core level spectra were acquired at kinetic energy of 530 eV and different potentials as indicated in the figures. All data are obtained at RT under 3 mbar H_2O ambient in the NAP-XPS chamber.*

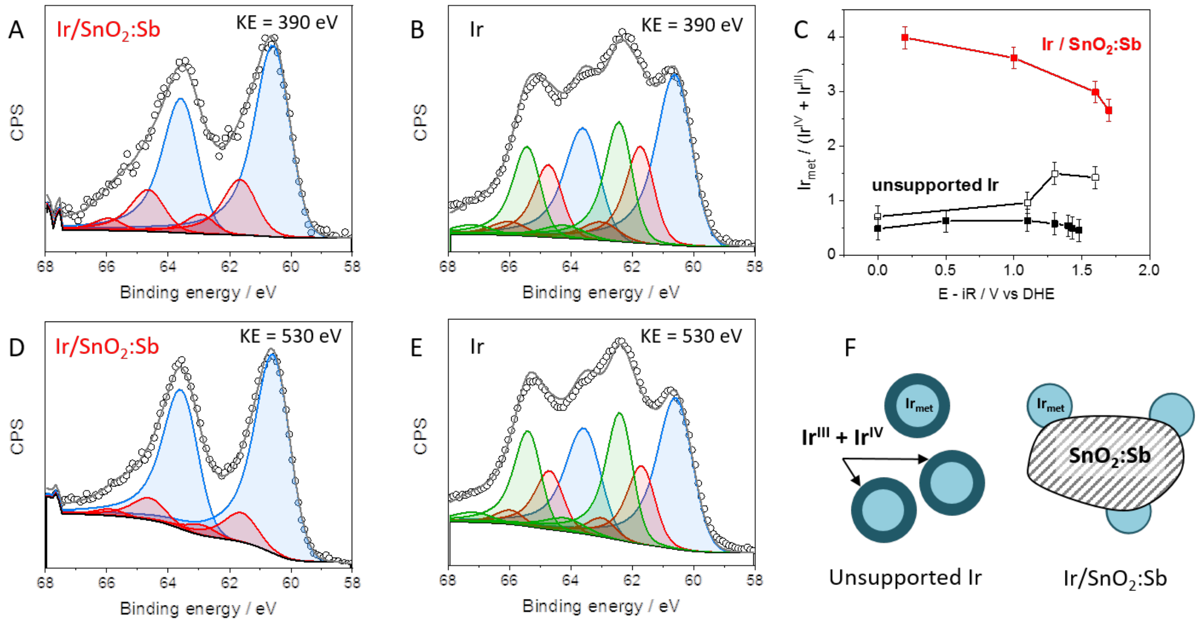

Figure 2. *Ir4f XP spectra for Ir/SnO$_2$:Sb (A, D) and unsupported Ir (B, E) recorded after potential cycling (see Methods) at potential close to the open circuit at kinetic energies of 390 eV (A, B) and 530 eV (D, E). Colour codes: metallic Ir – blue, Ir(IV) and its satellite – red, Ir(III) and its satellite - green. Experimental results are shown as circles, fitting as a grey line. Fitting was performed considering five doublets (see Table S1-S3): metallic Ir with Ir 4f$_{7/2}$ at 60.6 eV, Ir(III) at 62.5 eV, Ir(III) satellite at 64.4 eV, Ir(IV) at 62.0 eV and Ir(IV) satellite at 63.3 eV. Data for unsupported Ir are replotted from Ref.*[33] *Panel (C) shows the atomic ratio of metallic to oxidised Ir for Ir/SnO$_2$:Sb (red) and unsupported Ir (black) at different electrode potentials. Results for unsupported Ir obtained at BESSY (full symbols) and SOLEIL (open symbols) synchrotron facilities are replotted from Refs.*[20,33] *All data were obtained at RT under 3 mbar H$_2$O ambient in a NAP-XPS chamber. Note that the potential scale in Ref.*[33] *was shifted and for the sake of comparison is corrected by adding +0.25 V. The error bars were estimated based on the fitting parameters variations of the corresponding spectra. Panel F schematically illustrates the difference between supported and unsupported Ir catalysts.*

Figure 2C shows the atomic ratios of metallic to oxidized Ir (calculated as a sum of Ir(IV) and Ir(III)) as a function of the electrode potential for the SnO$_2$:Sb -supported and unsupported Ir. The most striking is a noticeably higher Ir metal contribution for Ir/SnO$_2$:Sb than for unsupported Ir in the entire studied potential interval. XP spectra modelling (see Figure S15) allows estimating the apparent thickness of the oxide layer as ca. 0.3-0.4 nm under the OER conditions. This is significantly smaller than the value estimated for unsupported Ir nanoparticles (0.6 and 0.7 nm under the OER conditions in Ref.[33] and Ref.[20] respectively). Our conclusion on a thinner IrO$_x$ layer on Ir/SnO$_2$:Sb compared to unsupported Ir is in agreement with Ref.[15], even if the extent of Ir oxidation and thus the oxide thickness was significantly higher in Ref.[15]. However, the conclusion of *Oh et al.*[15] on the Ir oxidation state being close to +3 does not agree with current results rather evidencing absence of Ir(III) species in Ir/SnO_2:Sb.

Summing up, the differences between SnO_2:Sb-supported and unsupported Ir nanoparticles manifested in (i) a thinner IrO_x layer and (ii) the absence of Ir(III) contribution for the former. It was recently suggested that degradation of active Ir-based catalysts under OER conditions make takes place *via* formation of intermediates in the oxidation state Ir(III).[34] Considering this, the decrease in the contribution of Ir(III) for the SnO_2:Sb supported sample, revealed by NAP-XPS, explains the difference in the dissolution behaviour in supported and unsupported samples in Figure 3. We attribute these dissolution differences to the Ir-SnO_2:Sb interaction discussed below.

Stability towards dissolution. Dissolution of unsupported Ir and Ir/SnO_2:Sb-based catalysts during the OER, studied under galvanostatic conditions, is compared in Figure 3. Dissolution of unsupported Ir is fast in the beginning of the measurements but slows down considerably after 500 min, the overall amount of dissolved Ir reaching ca. 3 % of the loaded metal. Such a behaviour may be attributed to a gradual passivation of the surface of metallic Ir nanoparticles as recently described by *Li et al.*[21] The rate of the Ir dissolution in Ir/SnO_2:Sb is noticeably smaller at the start of the measurements, approaching steady-state. In the timeframe of the experiment, the state-state was not reached. Sb and Sn of the support are also subject to dissolution as may be seen from Figure 3B, which demonstrates preferential dissolution of Sb in agreement with *Geiger et al.*[27] and *Fabbri et al.*[28] who studied degradation of SnO_2:Sb under anodic polarization in acid. Decrease in the Ir dissolution rate and slower establishment of a steady state in Ir/SnO_2:Sb compared to the unsupported Ir indicate slowly ongoing compositional changes in the surface layers of the electrode. Such behaviour can be explained by slow oxidation of the surface of metallic Ir nanoparticles in the SnO_2:Sb-based sample under the OER conditions and corresponds to our findings using *operando* NAP-XPS measurements.

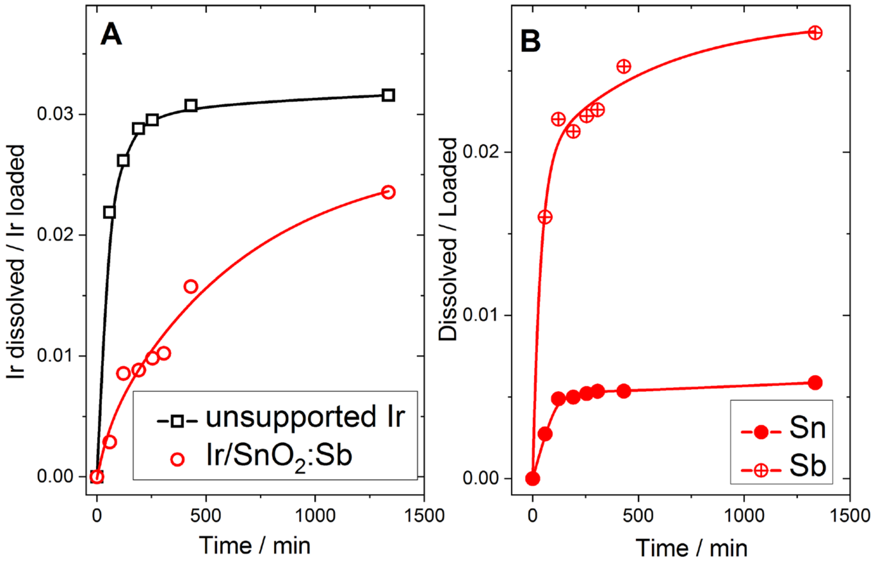

Figure 3. *Time dependence of the amount of dissolved Ir (A), Sn and Sb (B) during anodic polarization of unsupported Ir (black in A) and supported Ir/*SnO_2*:Sb -based (red in A, B) catalysts under galvanostatic conditions at 1 mA cm*$^{-2}$ *in 0.1 M* H_2SO_4 *using H-cell with divided anodic and cathodic compartments.*

Metal-support interaction evidenced by *operando* NAP-XPS. We seek to further understand the Ir-SnO_2:Sb interaction by exploring the Sn3$d_{5/2}$ binding energy and the Sn/Ir atomic ratio values. For the bare support, the Sn3$d_{5/2}$ binding energy is 487.3 ± 0.2 eV (Figure S3), which is in agreement with the previous publications and is higher than the value reported for undoped SnO_2. This binding energy increase has been attributed to the shrinkage of the band gap and screening of the Coulomb repulsion between valence and conduction electrons (see Ref.[35] and references therein). For bare SnO_2:Sb the Sn3$d_{5/2}$ binding energy does not show noticeable dependence either on the electrode potential or the kinetic energy of the photoelectrons (Figure S3), suggesting that a potentially induced Schottky barrier at the SnO_2:Sb/electrolyte interface[36] is not very significant. However, increase of the electrode potential for Ir/SnO_2:Sb leads to a small but systematic decrease of the Sn3d binding energy (Figure 2E and Figure S5), the latter approaching the value characteristic of undoped SnO_2. Since we observed only less than 3% loss of Sb (Fig. 3B), the observed shift of the Sn3d peak could not be attributed to the Sb loss. Hence, in order to explain both the decrease of the binding energy of Sn3d with potential, and a significantly lower extent of oxidation of SnO_2:Sb-supported compared to unsupported Ir nanoparticles, we suggest oxygen atom spill-over from Ir nanoparticles to the SnO_2:Sb support resulting in the oxygen vacancy filling (for the role of oxygen vacancies in doped and undoped SnO_2 the reader is referred to Ref.[35] and references therein). As the electrode potential increases, following processes likely occur at the Ir/SnO_2 anode. First, electrochemisorption and dissociation of water proceeds on the surface of Ir:

$H_2O + [\ ]_{Ir} \rightarrow O_{ads,Ir} + 2H^+ + 2e^-$ (1)

Here $[]_{Ir}$ stands for a vacant site on the surface of an Ir nanoparticle. Further increase of the electrode potential results in surface oxidation (2) evidenced by NAP-XPS.

$xO_{ads,Ir} + Ir_{surf} \rightarrow IrO_{x,surf}$ (2)

A significantly smaller level of surface oxidation in SnO_2:Sb-supported Ir compared to that in unsupported Ir suggests that some oxygen atoms adsorbed on Ir ($O_{ads,Ir}$) spill-over to the SnO_2:Sb support resulting in a partial oxygen vacancy ($V_O^{\cdot\cdot}$) filling:

$O_{ads,Ir} + V_O^{\cdot\cdot} + 2e^- \rightarrow O_O^x$ (3)

Step (3) results in a decrease of the electron population of the conduction band of SnO_2:Sb leading to a band gap opening[37] and ensuing decrease of the Sn3d binding energy. Note that quantum chemical calculations suggest stabilization of the oxygen vacancies at the metal-semiconductor interface[38]. Oxygen atoms from the Ir/SnO_2:Sb interface can diffuse along the surface and into the bulk of the SnO_2:Sb nanoparticles. This is schematically illustrated in Figure 4.

The analysis of Sn/Ir atomic ratio (Figure S7) revealed its increase with the applied potential. For supported nanoparticles such a behavior is often related to back spill-over of the support moieties to metal nanoparticles resulting in an encapsulation of the latter[39]. On the other hand, it could also originate from detachment, agglomeration or change in the shape of Ir nanoparticles. However, none of these phenomena were confirmed by post-mortem microscopic analysis of the Ir/SnO_2:Sb-based anodes. Thus, the question regarding the physical origin for the observed increase of the Sn/Ir ratio remains open. For further details, the reader is referred to the SI.

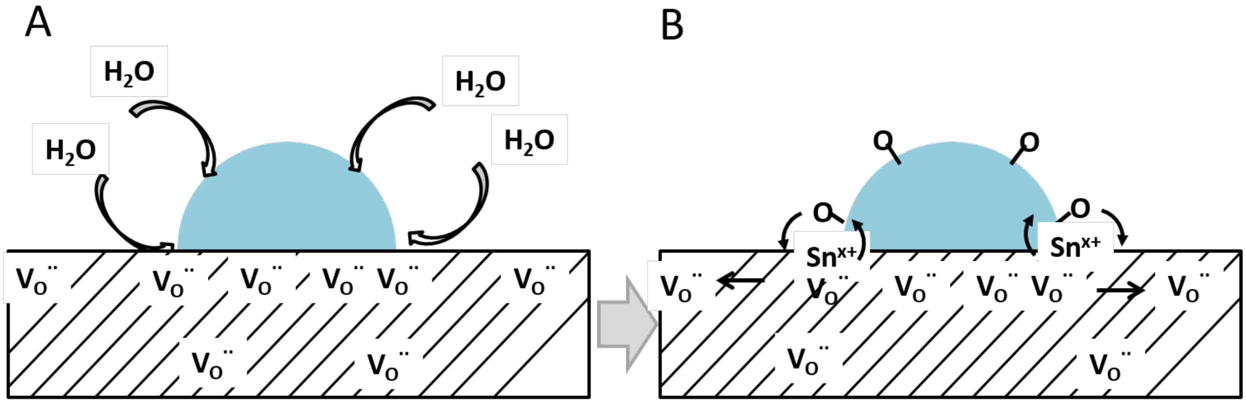

Figure 4. *Schematic representation of the oxygen spill-over to the SnO_2:Sb support under anodic polarization: electrochemisorption and dissociation of water on the surface of Ir (panel A) followed by adsorbed oxygen spill-over from Ir to the SnO_2:Sb support resulting in partial oxygen vacancy refilling (panel B).*

In summary, this study provides an insight into the mechanisms that lead to high electrocatalytic activity and stability of Ir supported on SnO_2:Sb-aerogel compared to the unsupported Ir. By applying *operando* NAP-XPS on a PEMWE cell, we present evidence for a lower degree of Ir oxidation in the Ir/SnO_2:Sb anodes compared to the unsupported ones, which is attributed to the oxygen spill-over from Ir to the support and results in a thinner layer of Ir oxide on the surface of Ir nanoparticles. NAP-XPS evidences diminution of the Ir(III) fraction, the latter considered an intermediate in the Ir dissolution process. The mitigation of Ir dissolution for Ir/SnO_2:Sb compared to unsupported Ir under constant load is confirmed by ICP-MS. In overall, our results demonstrate that there is a way to evade the rule which states that for having highly active Ir catalysts there is always a compromise in stability.[40] In this regard, the use electro-ceramic aerogel supports might be the key for enabling sustainable PEMWE at the terawatt scale for decarbonising the hydrogen industry.

Methods

Ir/SnO_2:Sb Synthesis. The SnO_2:Sb aerogels with the Sn/Sb atomic ratio 10:1 were prepared by an acid-catalyzed sol–gel route starting with metal alkoxides, tin isopropoxide (Alfa Aesar, 99% (metals basis)) and antimony (III) isopropoxide (Alfa Aesar, 99.9% (metals basis)), as precursors[41]. To prepare SnO_2:Sb-supported Ir catalyst (30 wt.% Ir), the SnO_2:Sb aerogel was added to $IrCl_3$-containing anhydrous ethanol followed by $NaBH_4$ reduction[30].

MEA preparation. The MEAs were fabricated similar to the procedure published in [20,33] by wet spraying method using E87-05S Aquivion membrane and D72-25BS dispersion (Solvay). The inks were prepared by dispersing the catalyst powders in 20 wt. % of Aquivion dispersion in isopropyl alcohol (AMRESCO) and ultra-pure water with the ratio of 1:1. The anode or working electrode contained either Ir/SnO_2:Sb (with Ir loading of 0.5 mg cm^{-2}) or, for the sake of comparison, SnO_2:Sb (with the loading set at 0.5 mg cm^{-2}). Nitrogen-doped reduced graphite oxide, prepared by high temperature pyrolysis from a Polypyrrole/Graphite oxide composite[42], was added (50 wt. %) to the suspension to improve the in-plane electrical conductivity of the resulting catalyst layer (see section 2 of Supporting Information). For the cathode or counter electrode, HiSPEC4000 Pt/C (40 wt. % Pt from Johnson Matthey) with the platinum loading of 1 mg cm^{-2} was applied. The high Pt loading of the counter electrode was chosen intentionally in order to minimize overpotential of the hydrogen evolution reaction. After spraying, the MEAs were hot pressed. The geometric area of the electrodes was 0.9 cm^2.

Dissolution measurements. The stability measurements were performed in galvanostatic conditions applying 1 mA cm^{-2} (Gamry Reference 600, USA) to the electrodes until steady-state was achieved. The experiments were performed in the H-cell with anodic and cathodic compartments divided by a fine glass frit (Pine Research Instrumentation, USA). A carbon rod in the cathodic compartment and saturated Ag/AgCl in the anodic compartment were used as counter and reference electrodes, respectively. The working electrodes were prepared by drop casting on the gold substrate of 40 μL of the suspensions containing 1 mg mL^{-1} of a catalyst. The geometric area of working electrodes was 0.4 cm^{-2}. Dissolution was normalized to the loading of Ir in the electrode. The volume of electrolyte in both compartments of the H-cell was adjusted to 20 mL and was kept constant during the measurements. At various durations of electrolysis 1 mL aliquot of the electrolyte from the anodic compartment was sampled and further analyzed using an inductively coupled plasma mass spectrometer (ICP-MS, NexION 300X, Perkin Elmer). Prior to introduction into the ICP-MS the aliquot was mixed with an internal standard (10 μg L^{-1}) and the total volume was adjusted to 10 mL. As internal standards solutions of Rh and Re were used for detection of Sn, Sb and Ir, respectively. The ICP-MS was calibrated prior to the analysis.

***Ex situ* TEM/STEM/EDX characterisation**. The analysis of the particle shape and size distributions as well as the elemental mapping were performed by TEM and STEM-EDX analysis. In order to study the electrocatalyst particles after the *operando* measurements, the corresponding working electrode sides of the membrane electrode assemblies were scratched with a diamond pen and the obtained powders were transferred to a copper grid for further microscopy measurements. TEM images, HAADF-STEM images and energy dispersive X-ray maps were acquired using a FEI Titan 80-300 "cubed" microscope equipped with a Super-X detector and operated at 300 kV. The probe current was 150 pA. Sn-L (3.44 keV), Sb-L (3.50 keV), Ir-L (9.17 keV) and O-K (0.52 keV) lines were used for the chemical maps.

***Operando* NAP-XPS measurements.** The experiments were carried out using the NAP-XPS from the Sorbonne University (France) installed at the TEMPO beamline[43] at room temperature using two-electrode cell configuration under 3 mbar water vapor pressure similar to what has been described by *Saveleva et al.*[44]. Gas composition was controlled by online mass spectrometry. The OER onset potential observed in the two-electrode cell was close to the value measured in a three-electrode cell vs. reversible hydrogen electtrode, suggesting that the counter Pt/C electrode can be considered as a dynamic hydrogen electrode (DHE) as it was explained by *Saveleva et al.*[44] The evolution of oxygen was controlled by the on-line mass spectrometry (the data are not shown). A μ-AutoLab potentiostat (Metrohm) was used for controlling the electrode potential and for performing cyclic voltammetry, electrochemical impedance spectroscopy, and chronoamperometry measurements. Photoemission spectra were acquired under constant voltage applied between the working electrode and the counter electrode in the interval from 0.2 V (lower potential were not applied to avoid cathodic SnO_2:Sb degradation described in the literature[27]) to 1.7 V. The corresponding chronoamperograms are shown in Figure 2B and S1. Ir4f, Sn3d, Sb3d and O1s XP spectra were collected at kinetic energy of the emitted electrons of ca. 390 eV, 530 eV and 810 eV and pass energy 50 eV for Ir4f and 20 eV for the others. These values correspond to the analytical depths of 1.9 nm, 2.3 nm, 3.6 nm, respectively, calculated as three times the inelastic mean free path (IMFP) estimated for metallic iridium. Spectra for other elements present on the electrode surface (C1s, F1s, S2p) were acquired at a kinetic energy of 530 eV. The binding energy calibration was done by the position of the metallic iridium component in the Ir4f spectra. The surface SnO_2:Sb atomic ratios were calculated from the spectral intensities normalized by the energy dependent incident photon flux and the photoelectric cross-section taken from[45].

NAP-XPS experiments performed without addition of graphene to the working electrode layer showed potential-induced binding energy shifts of Ir4f, Sn3d and Sb3d peaks evidencing poor conductivity of the catalytic layer (Figure S2, panel A). This problem was rectified upon addition of N-doped reduced graphene oxide (Figure S2, panel B).

Before performing NAP-XPS measurements, the electrodes were subjected to potential cycling in the potential region prior to the OER onset [0.2; 1.0] V vs. DHE with s. Electrochemical characteristics of MEAs were controlled during the measurements by means of CV and EIS. Typical CVs and chronoamperograms for SNO2:SB and Ir-SNO2:SB WEs recorded in the NAP-XPS chamber in presence of water vapor are shown in Figures S1 and panels A, B of Figure 2, correspondingly.

Ir4f XP spectra: fitting procedure. Fitting of Ir4f XP spectra was based on the parameters described in *Pfeifer et al.*[46] The fit parameters are shown in Table S1-S3 of the SI. The assignment of Ir components was based on the literature data (see Table S3 in *Saveleva et al.*[44]). Background subtraction was carried out using the Shirley method and the asymmetric Doniach-Sunjic line shape was used for the fitting. The peak separation and the peak area ratios between the Ir4f$_{7/2}$ and the Ir4f$_{5/2}$ components were constrained to 3 eV and 4:3, respectively. The area ratio between the main core-level peak and the satellite 1 and 2 was maintained constant and was equal to 5.6 and 11.1, respectively.

SESSA simulations. In order to reproduce the potential-induced effects observed experimentally, modelling of the corresponding photoemission spectra was performed using SESSA software (Version 2.0).[47] The configurations of the sample, analyzer etc. have been selected close to the real set-up used at the TEMPO beamline and shown in Table S5 of SI. The sketch of the morphology used for the calculations of SnO_2:Sb supported Ir-based systems as well as the applied parameters are presented in Figure S16.

Associated content

Supporting information

Additional experimental data, fitting procedures, photoemission spectra simulation. This information is available free of charge on the ACS Publications website.

Author Contributions

A.S.G. and K.A.F. initiated the project. V.A.S., E.S. and S.Z. designed NAP-XPS experiments. V.A.S. E.R.S., S.Z., J.-J.G. and F.B. performed NAP-XPS measurements, V.A.S. carried out the XPS data analysis. L.W. synthesized catalysts and performed liquid-phase electrochemical measurements. L.W. and V.A.S. prepared MEAs. O.K., S.C. and K. J.J.M. performed Ir/SNO2:SB stability measurements. M.B. and J.H. performed *ex situ* TEM/STEM/EDX characterization. G.O. and C.B. prepared SnO_2:SB aerogels. N.A.-V. prepared nitrogen-doped rGO samples. V.A.S. and E.R.S wrote the manuscript, which all authors edited. All authors discussed the results and their interpretation.

Acknowledgements

The research leading to these results has received funding from the European Union's Seventh Framework Program (FP7/2007-2013) for Fuel Cell and Hydrogen Joint Technology (FCH JU) Initiative under Grant No. 621237 (INSIDE). In addition, A.S.G. and C.B. thank the European Union's Horizon 2020 research and innovation programme for funding the project PRETZEL under grant agreement No 779478 and it is supported by FCH JU. Solvay is acknowledged for providing Aquivion membrane and ionomer.

References

(1) Haubner, B.; Pitschak, B.; Bayer, A.; Gago, A.; Lettenmeier, P.; Christoph, V.; Smolinka, T. Wie Kommen Wind Und Sonne Ins Gasnetz ? *DVGW* **2017**, 12–16.

(2) EU project REFHYNE, https://refhyne.eu/. Accessed on January 18th, 2020.

(3) Air Liquide Hydrogen Energy, https://www.airliquide.com/science-new-energies/hydrogen-energy. Accessed on January 18th, 2020.

(4) PV Magazine, https://www.pv-magazine.com/2019/02/12/amprion-and-oge-announce-100-mw-power-to-gas-project-in-germany/. Accessed on January 18th, 2020.

(5) K.A.Friedrich, PlanDelyKad: Study on Large Scale Water Electrolysis and Hydrogen Storage (in German). German Federal Ministry for Economic Affairs and Energy (BMWi), Berlin (2015), http://edok01.tib.uni-hannover.de/edoks/e01fb15/824812212.pdf. Accessed on January 18th, 2020.

(6) Carmo, M.; Fritz, D. L.; Mergel, J.; Stolten, D. A Comprehensive Review on PEM Water Electrolysis. *Int. J. Hydrogen Energy* **2013**, *38*, 4901–4934.

(7) Bloomberg, https://www.bloomberg.com/news/articles/2018-04-27/rally-in-rarest-precious-metal-hots-up-as-prices-hit-record. Accessed on January 18th, 2020.

(8) Ayers, K.; Danilovic, N.; Ouimet, R.; Carmo, M.; Pivovar, B.; Bornstein, M. Perspectives

on Low-Temperature Electrolysis and Potential for Renewable Hydrogen at Scale. *Annu. Rev. Chem. Biomol. Eng.* **2019**, *10*, 219–239.

(9) Johnson Matthey, PGM Market Report February 2019, http://www.platinum.matthey.com/documents/new-item/pgm%20market%20reports/pgm_market_report_february_2019.pdf. Accessed on January 18th, 2020.

(10) Paoli, E. A.; Masini, F.; Frydendal, R.; Deiana, D.; Schlaup, C.; Malizia, M.; Hansen, T. W.; Horch, S.; Stephens, I. E. L.; Chorkendorff, I. Oxygen Evolution on Well-Characterized Mass-Selected Ru and RuO_2 Nanoparticles. *Chem. Sci.* **2015**, *6*, 190–196.

(11) Nong, H. N.; Oh, H.-S. S.; Reier, T.; Willinger, E.; M.G., W.; Petkov, V.; Teschner, D.; Strasser, P.; Willinger, M.-G. G.; Petkov, V.; Teschner, D.; Strasser, P. Oxide-Supported IrNiOx Core-Shell Particles as Efficient, Cost-Effective, and Stable Catalysts for Electrochemical Water Splitting. *Angew. Chemie - Int. Ed.* **2015**, *54*, 2975–2979.

(12) Wang, L.; Saveleva, V. A.; Zafeiratos, S.; Savinova, E. R.; Lettenmeier, P.; Gazdzicki, P.; Gago, A. S.; Friedrich, K. A. Highly Active Anode Electrocatalysts Derived from Electrochemical Leaching of Ru from Metallic Ir0.7Ru0.3 for Proton Exchange Membrane Electrolyzers. *Nano Energy* **2017**, *34*, 385–391.

(13) Cherevko, S.; Geiger, S.; Kasian, O.; Kulyk, N.; Grote, J.; Savan, A.; Ratna, B.; Merzlikin, S.; Breitbach, B.; Ludwig, A.; Mayrhofer, K. J. J. Oxygen and Hydrogen Evolution Reactions on Ru , RuO2 , Ir , and IrO2 Thin Film Electrodes in Acidic and Alkaline Electrolytes : A Comparative Study on Activity and Stability. *Catal. Today* **2016**, *262*, 170–180.

(14) Danilovic, N.; Subbaraman, R.; Chang, K. C.; Chang, S. H.; Kang, Y. J.; Snyder, J.; Paulikas, A. P.; Strmcnik, D.; Kim, Y. T.; Myers, D.; Stamenkovic, V. R.; Markovic N. M. Activity-Stability Trends for the Oxygen Evolution Reaction on Monometallic Oxides in Acidic Environments. *J. Phys. Chem. Lett.* **2014**, *5*, 2474–2478.

(15) Oh, H.; Nong, H. N.; Reier, T.; Bergmann, A.; Gliech, M.; Ferreira, J.; Arau, D.; Willinger, E.; Schlo, R.; Teschner, D.; Strasser, P. Electrochemical Catalyst − Support Effects and Their Stabilizing Role for IrOx Nanoparticle Catalysts during the Oxygen Evolution Reaction. *J. Am. Chem. Soc.* **2016**, *138*, 12552–12563.

(16) Claudel, F.; Dubau, L.; Berthomé, G.; Sola-Hernandez, L.; Beauger, C.; Piccolo, L.; Maillard, F. Degradation Mechanisms of Oxygen Evolution Reaction Electrocatalysts: A Combined Identical-Location Transmission Electron Microscopy and X-Ray Photoelectron Spectroscopy Study. *ACS Catal.* **2019**, *9*, 4688–4698.

(17) Wang, L.; Lettenmeier, P.; Golla-Schindler, U.; Gazdzicki, P.; Cañas, N.; Handl, M.; Hiesgen, R.; Hosseiny, S. S.; Gago, A. S.; Friedrich, A. K. Nanostructured Ir-Supported on Ti4O7 as Cost Effective Anode for Proton Exchange Membrane (PEM) Electrolyzers. *Phys. Chem. Chem. Phys.* **2015**, *18*, 4487–4495.

(18) Lettenmeier, P.; Wang, L.; Golla-Schindler, U.; Gazdzicki, P.; Cañas, N. A.; Handl, M.; Hiesgen, R.; Hosseiny, S. S.; Gago, A. S.; Friedrich, K. A. Nanosized IrOx -Ir Catalyst with Relevant Activity for Anodes of Proton Exchange Membrane Electrolysis Produced by a Cost-Effective Procedure. *Angew. Chem. Int. Ed. Engl.* **2016**, *128*, 752–756.

(19) Cherevko, S.; Reier, T.; Zeradjanin, A. R.; Pawolek, Z.; Strasser, P.; Mayrhofer, K. J. J. Stability of Nanostructured Iridium Oxide Electrocatalysts during Oxygen Evolution Reaction in Acidic Environment. *Electrochem. commun.* **2014**, *48*, 81–85.

(20) Saveleva, V. A.; Wang, L.; Teschner, D.; Jones, T. E.; Gago, A. S.; Friedrich, K. A.; Zafeiratos, S.; Schloegl, R.; Savinova, E. R. Operando Evidence for a Universal Oxygen Evolution Mechanism on Thermal and Electrochemical Iridium Oxides. *J. Phys. Chem. Lett.* **2018**, *9*, 3154–3160.

(21) Li, T.; Kasian, O.; Cherevko, S.; Zhang, S.; Geiger, S.; Scheu, C.; Felfer, P.; Raabe, D.; Gault, B.; Mayrhofer, K. J. J. Atomic-Scale Insights into Surface Species of Electrocatalysts in Three Dimensions. *Nat. Catal.* **2018**, *1*, 300–305.

(22) Moradi, F.; Dehghanian, C. Addition of IrO2 to RuO2+TiO2 Coated Anodes and Its Effect on Electrochemical Performance of Anodes in Acid Media. *Prog. Nat. Sci. Mater. Int.* **2014**, *24*, 134–141.

(23) Aizawa, M.; Lee, S.; Anderson, S. L. Deposition Dynamics and Chemical Properties of Size-Selected Ir Clusters on TiO2. *Surf. Sci.* **2003**, *542*, 253–275.

(24) Walsh, F. C.; Wills, R. G. A. The Continuing Development of Magneli Phase Titanium Sub-Oxides and Ebonex (R) Electrodes. *Electrochim. Acta* **2010**, *55*, 6342–6351.

(25) Wickman, B.; Wesselmark, M.; Lagergren, C.; Lindbergh, G. Tungsten Oxide in Polymer Electrolyte Fuel Cell Electrodes — A Thin-Film Model Electrode Study. *Electrochim. Acta* **2011**, *56*, 9496–9503.

(26) Liu, G.; Xu, J.; Wang, X. An Oxygen Evolution Catalyst on an Antimony Doped Tin Oxide Nanowire Structured Support for Electrolysis. *J. Mater. Chem. A Mater. energy Sustain.* **2015**, *3*, 20791–20800.

(27) Geiger, S.; Kasian, O.; Mingers, A. M.; Mayrhofer, K. J. J.; Cherevko, S. Stability Limits of Tin-Based Electrocatalyst Supports Stability Limits of Tin-Based Electrocatalyst Supports. *Sci. Rep.* **2017**, *7*, 4595–4602.

(28) Fabbri, E.; Rabis, A.; Ko, R.; Schmidt, T. J. Pt Nanoparticles Supported on Sb-Doped SnO2 Porous Structures : Developments and Issues. *PCCP* **2014**, *16*, 13672–13681.

(29) Oh, H.-S.; Nong, H. N.; Reier, T.; Gliech, M.; Strasser, P. Oxide-Supported Ir Nanodendrites with High Activity and Durability for the Oxygen Evolution Reaction in Acid PEM Water Electrolyzers. *Chem. Sci.* **2015**, *6*, 3321–3328.

(30) Wang, L.; Song, F.; Ozouf, G.; Geiger, D.; Morawietz, T.; Handl, M.; Gazdzicki, P.; Beauger, C.; Kaiser, U.; Hiesgen, R.; Gago, A. S.; Friedrich, K. A. Improving the Activity and Stability of Ir Catalysts for PEM Electrolyzer Anodes by SnO2 : Sb Aerogel Supports : Does V Addition Play an Active Role in Electrocatalysis? *J. Mater. Chem. A Mater. energy Sustain.* **2017**, *5*, 3172–3178.

(31) Ohno, H.; Nohara, S.; Kakinuma, K.; Uchida, M.; Uchida, H. Effect of Electronic Conductivities of Iridium Oxide/Doped SnO2 Oxygen-Evolving Catalysts on the Polarization Properties in Proton Exchange Membrane Water Electrolysis. *Catalysts* **2019**, *9*, 74–86.

(32) Solà-Hernández, L.; Claudel, F.; Maillard, F.; Beauger, C. Doped Tin Oxide Aerogels as Oxygen Evolution Reaction Catalyst Supports. *Int. J. Hydrogen Energy* **2019**, *44*, 24331–24341.

(33) Lettenmeier, P.; Majchel, J.; Wang, L.; Saveleva, V. A.; Zafeiratos, S.; Savinova, E.; Gallet, J.-J.; Bournel, F.; Gago, A. S.; Friedrich, K. A. Highly Active Nano-Sized Iridium Catalysts: Synthesis and Operando Spectroscopy in Proton Exchange Membrane Electrolyzer. *Chem. Sci.* **2018**, *9*, 3570–3579.

(34) Cherevko, S.; Geiger, S.; Kasian, O.; Mingers, A.; Mayrhofer, K. J. J. Oxygen Evolution Activity and Stability of Iridium in Acidic Media . Part 2 . – Electrochemically Grown Hydrous Iridium Oxide. *JEAC* **2016**, *774*, 102–110.

(35) Batzill, M.; Diebold, U. The Surface and Materials Science of Tin Oxide. *Prog. Surf. Sci.* **2005**, *79*, 47–154.

(36) Binninger, T.; Mohamed, R.; Patru, A.; Waltar, K.; Gericke, E.; Tuaev, X.; Fabbri, E.; Levecque, P.; Hoell, A.; Schmidt, T. J. Stabilization of Pt Nanoparticles Due to Electrochemical Transistor Switching of Oxide Support Conductivity. *Chem. Mater.* **2017**, *29*, 2831–2843.

(37) Schipani, F.; Ponce, M. A.; Joanni, E.; Williams, F. J.; Aldao, C. M. Study of the Oxygen Vacancies Changes in SnO2 Polycrystalline Thick Films Using Impedance and Photoemission Spectroscopies. *J. Appl. Phys.* **2014**, *116*, 194502–194510.

(38) Puigdollers, A. R.; Schlexer, P.; Tosoni, S.; Pacchioni, G. Increasing Oxide Reducibility: The Role of Metal/Oxide Interfaces in the Formation of Oxygen Vacancies. *ACS Catal.* **2017**, *7*, 6493–6513.

(39) Fu, Q.; Wagner, T.; Olliges, S.; Carstanjen, H. D. Metal-Oxide Interfacial Reactions: Encapsulation of Pd on TiO2 (110). *J. Phys. Chem. B* **2005**, *109*, 944–951.

(40) Geiger, S.; Kasian, O.; Ledendecker, M.; Pizzutilo, E.; Mingers, A. M.; Fu, W. T.; Diaz-Morales, O.; Li, Z.; Oellers, T.; Fruchter, L.; Ludwig, A.; Mayrhofer, K. J. J.; Koper, M. T. M.; Cherevko, S. The Stability Number as a Metric for Electrocatalyst Stability Benchmarking. *Nat. Catal.* **2018**, *1*, 508–515.

(41) Ozouf, G.; Beauger, C. Niobium- and Antimony-Doped Tin Dioxide Aerogels as New Catalyst Supports for PEM Fuel Cells. *J. Mater. Sci.* **2016**, *51*, 5305–5320.

(42) García-Rosado, I. J.; Uribe-Calderón, J.; Alonso-Vante, N. Nitrogen-Doped Reduced Graphite Oxide as a Support for CoSe Electrocatalyst for Oxygen Reduction Reaction in Alkaline Media. *J. Electrochem. Soc.* **2017**, *164*, F658–F666.

(43) Polack, F.; Silly, M.; Chauvet, C.; Lagarde, B.; Bergeard, N.; Izquierdo, M.; Chubar, O.; Krizmancic, D.; Ribbens, M.; Duval, J. P.; Basset, C.; Kubsky, S., Sirotti, F. TEMPO : A New Insertion Device Beamline at SOLEIL for Time Resolved Photoelectron Spectroscopy Experiments on Solids and Interfaces TEMPO : A New Insertion Device Beamline at SOLEIL for Time Resolved Photoelectron Spectroscopy Experiments on Solids and In. *AIP Conf. Proc.* **2010**, *1234*, 1–5.

(44) Saveleva, V. A.; Wang, L.; Luo, W.; Zafeiratos, S.; Ulhaq-Bouillet, C.; Gago, A. S.; Friedrich, K. A.; Savinova, E. R. Uncovering the Stabilization Mechanism in Bimetallic Ruthenium–Iridium Anodes for Proton Exchange Membrane Electrolyzers. *J. Phys. Chem. Lett.* **2016**, *7*, 3240–3245.

(45) Yeh, J. J. *Atomic Calculation of Photoionization Cross-Sections and Asymmetry Parameters*; Gordon & Breach Science, 1993.

(46) Pfeifer, V.; Jones, T. E.; Velasco Vélez, J.-J.; Greiner, M.; Massué, C.; Arrigo, R.; Teschner, D.; Girgsdies, F.; Scherzer, M.; Allan, J.; Hashagen, M.; Weinberg, G.; Piccinin, S; Haevecker, M.; Knop-Gericke, A., Schloegl, R. The Electronic Structure of Iridium Oxide

Electrodes Active in Water Splitting. *Phys. Chem. Chem. Phys.* **2016**, *18*, 2292–2296.

(47) Werner, W. S. M.; Smekal, W.; Hisch, T.; Himmelsbach, J.; Powell, C. J. Simulation of Electron Spectra for Surface Analysis (SESSA) for Quantitative Interpretation of (Hard) X-Ray Photoelectron Spectra (HAXPES). *J. Electron Spectros. Relat. Phenomena* **2013**, *190*, 137–143.

For Table of Contents Only